Nuclear and Neutron Matter Calculations with Different Model Spaces

L. Engvik, E. Osnes

Department of Physics, University of Oslo, N-0316 Oslo, Norway

M. Hjorth-Jensen

Nordita, Blegdamsvej 17, DK-2100 København Ø, Denmark

T.T.S. Kuo

Department of Physics, State University of New York at Stony Brook, NY 11794, USA

Abstract

In this work we investigate the so-called model-space Brueckner-Hartree-Fock (MBHF) approach for nuclear matter as well as for neutron matter and the extension of this which includes the particle-particle and hole-hole (PPHH) diagrams. A central ingredient in the model-space approach for nuclear matter is the boundary momentum k_M beyond which the single-particle potential energy is set equal to zero. This is also the boundary of the model space within which the PPHH diagrams are calculated. It has been rather uncertain which value should be used for k_M . We have carried out model-space nuclear matter and neutron matter calculations with and without PPHH diagrams for various choices of k_M and using several modern nucleon-nucleon potentials. Our results exhibit a saturation region where the nuclear and neutron matter matter energies are quite stable as k_M varies. The location of this region may serve to determine an "optimum" choice for k_M . However, we find that the strength of the tensor force has a significant influence on binding energy variation with k_M . The implications for nuclear and neutron matter calculations are discussed.

Key words: Nuclear Matter; Many-body correlations

1 Introduction

A common problem to non-relativistic nuclear matter calculations has been the simultaneous reproduction of both the binding energy per nucleon (BE/A =

 16 ± 1 MeV) and the saturation density $\rho_0 = 0.17$ fm⁻³. All modern realistic calculations of nuclear matter which employ two-body interactions such as Brueckner-like approaches [1–6], hyper-netted-chain [7] or coupled cluster [8] approaches are not able to reproduce in a satisfactory way the above nuclear matter data. If for a given interaction one is able to predict the saturation density, then the binding energy is underestimated. Similarly, if one is able to reproduce the binding energy of nuclear matter, then the saturation density is too high. This results in the so-called Coester band (see e.g. Fig. 3 below), where the saturation point for a given nucleon-nucleon (NN) interaction is correlated with the strength of the tensor force in the NN interaction.

In the past years relativistic approaches to nuclear matter have also been developed. For example, Brockmann and Machleidt [9,10] have recently shown, starting from a realistic NN interaction, that by performing a relativistic Dirac-Brueckner-Hartree-Fock (DBHF) nuclear matter calculation, one is able to meet the empirical nuclear matter data. Another line of approach is represented by the relativistic mean field scheme of Serot and Walecka [11]. However, the present relativistic approaches neglect the coupling to the negative energy solutions, and moreover relativistic approaches lead to a very small depletion of the Fermi sea [12]. This depletion is not consistent with recent (e, e'p) experiments.

Therefore, we believe that it is still worth to properly investigate non-relativistic schemes based on extensions of the Brueckner-Hartree-Fock (BHF) approach. One of the main problems with Brueckner theory is that particle states are treated differently from hole states. In the standard BHF approach one employs a discontinuous single particle (sp) spectrum, with a self-consistent BHF part for the nucleons below and a free-particle part above the Fermi surface. This leads to an unphysically large discontinuity of about 60 MeV for the sp spectrum at the Fermi level.

Several methods have been proposed to overcome this difficulty. Mahaux and his collaborators[6] used the real part of the reaction matrix to obtain a self-consistent sp spectrum which is continuous for all momenta. In the model-space Brueckner-Hartree-Fock (MBHF) approach proposed by Ma and Kuo[4] a continuous sp spectrum is obtained within a chosen model space (defined for momenta $k \leq k_M$), and the discontinuity at the model space boundary k_M is rather small for proper values of k_M . Although both methods yield more binding energy than the standard BHF approach, the nuclear matter empirical data are not reproduced. However, by including PPHH diagrams in the model space approach Song et al. [5] and Jiang et al. [13] have demonstrated that the saturation properties can be improved. Comparing with the standard hole-line expansion in BHF calculations, it is remarkable that the PPHH diagrams calculation can simultaneously increase the nuclear-matter binding energy and lower the saturation density ρ_0 .

A central question concerning the above PPHH-diagram nuclear matter approach is how to choose the boundary momentum k_M . In the past [5,13], one usually took a "reasonable" value for the size of the model space such as $k_M = 3.2 \text{ fm}^{-1}$ and proceeded to evaluate the nuclear matter PPHH diagrams. To our knowledge, PPHH-diagram nuclear matter calculations with other choices of k_M have not been investigated in a systematic way. Are there certain criteria which may help determine the boundary k_M ? Is there a saturation behavior in the sense that there exists a region where the results of PPHH-diagram nuclear matter calculations are insensitive to the choice of k_M ? The aim of this work is to study these questions. The answers to these questions may help confirm, or disconfirm, the rather encouraging results of the PPHH-diagram calculations reported earlier.

The reader should note that another way of summing PPHH diagrams has been developed by Dickhoff, Polls and Ramos, see e.g., Refs. [1–3]. There a self-consistent Green's function (SCGF) approach is used, where one solves the Dyson equation in order to get the sp Green's function. Although the sp energies are kept real in the self-consistency scheme, as in our case as well, the two methods differ in the treatment of the poles in the in-medium scattering matrix. In the model-space approach, see the discussion in the two next sections and Ref. [5], there are, by construction no poles at negative and positive starting energies in the effective interaction defined by the model-space reaction matrix. The poles from the retarded Green's function are circumvented by a contour integration [5]. One avoids thereby a numerically tedious evaluation of the two-body Green's function and effective interaction, as done in Refs. [1–3]. However, the SCGF method of Dickhoff, Polls and Ramos [1–3] allows one in a direct way to study other properties than just the binding energy. The one-body Green's functions can be used e.g., in the study of momentum distributions and spectral functions.

Finally, our scheme to obtain an effective interaction appropriate for nuclear matter starts with a free nucleon-nucleon interaction V which is appropriate for nuclear physics at low and intermediate energies. At present there are several potentials available. The most recent versions of Machleidt and co-workers [14], the Nijmegen group [15] and the Argonne group [16] have a χ^2 fit per datum close to 1. The potential model of Ref. [14] is an extension of the one-boson-exchange models of the Bonn group [9], where mesons like π , ρ , η , δ , ω and the fictitious σ meson are included. In the charge-dependent version of Ref. [14], the first five mesons have the same set of parameters for all partial waves, whereas the parameters of the σ meson are allowed to vary. The recent Argonne potential [16] is a charge-dependent version of the Argonne V14 [17] potential. The Argonne potential models are local potentials in coordinate space and include a π -exchange plus parameterizations of the short-range and intermediate range parts of the potential. The Nijmegen group [15] has constructed potentials based on meson exchange and models parameterized

in similar ways as the Argonne potentials. Another important difference between e.g., the Bonn potentials and the Argonne and Nijmegen potentials is the strength of the much debated tensor force [18]. Typically, the Bonn potentials have a smaller D-state admixture in the deuteron wave function than the Argonne and Nijmegen potentials, as well as other potential models. A smaller(larger) D-state admixture in the ground state of the deuteron means that the tensor force is weaker(stronger). The strength of the tensor force has important consequences in calculations of the binding energy for both finite nuclei and infinite nuclear matter, see e.g., the discussion in Ref. [19]. A potential model with a weak tensor force tends to yield more attraction in a nuclear system than a potential with a strong tensor force. The second aim of this work, is therefore to compare various nucleon-nucleon potentials, in order to study the role played by the tensor force. For this purpose we will work with three older versions of the Bonn potentials defined in table A.1 of ref. [9]. The only essential difference between these potentials is the relative strength of tensor force, which make the role of the tensor force more transparent in our investigation. They are recognized by the labels A, B and C with the former carrying the weakest tensor force. Such a set of potentials, fit to the same set of scattering data, allow us therefore to study the role played by the nuclear tensor force in a many-body approach like the present. Moreover, these potentials are constructed in exactly the same way, the only differences being the value of various meson variables (coupling constants, masses and cutoff energies). One may therefore be able to ascribe possible differences to the role played by certain mesons, or certain components of the NN interaction. In addition we have also done extensive calculations using the charge-dependent version of the Bonn potential models (CD-Bonn), see Ref. [14], and two potentials of the Nijmegen group [15], one meson-exchange potential (Nijm-OBE) and a local potential with a non-local contribution to the central force, i.e. the model Nijm-I of Ref. [15]. The reason for these choices is due to the fact that these potential models represent the most recent fits to the scattering data.

The PPHH-diagram nuclear matter calculations are closely related to the MBHF calculations, both employing a model space ($k \leq k_M$). In section 2 we will present the MBHF method and the results obtained with it. The basic method presented in section 2 is also used in the PPHH-diagram method discussed in section 3. The results of the PPHH-diagram calculations for nuclear and neutron matter are presented and discussed in sections 4 and 5, respectively. In section 6 we summarize and conclude.

2 Model Space Brueckner-Hartree-Fock Approach

The basic formalism of the MBHF has been exposed elsewhere, see e.g., Refs. [4,5]. Here we will therefore only briefly sketch the essential ingredients of the

method.

2.1 The Model Space G-matrix and Single-particle Spectrum

Following the conventional many-body approach, we rewrite the full Hamiltonian H = T + V, T being the kinetic energy and V the bare NN potential, in an unperturbed part $H_0 = T + U$ and an interacting part $H_I = V - U$ such that $H = T + V = H_0 + H_I$, where we have introduced an auxiliary sp potential U. If U is chosen such that H_I be small, perturbative many-body techniques can presumably be applied. A serious obstacle to any perturbative treatment is the fact that the bare NN potential V is very large at small internucleon distances, a fact which renders any perturbative approach highly prohibitive. To overcome this problem, one introduces the reaction matrix G, given by the solution of the integral equation

$$G_{ijkl}^{M}(\omega) = \bar{V}_{ijkl} + \sum_{m,n} \bar{V}_{ijmn} \frac{Q^{M}(m,n)}{\omega - (\epsilon_{m}^{M} + \epsilon_{n}^{M})} G_{mnkl}^{M}(\omega), \tag{1}$$

with the model-space Pauli exclusion operator

$$Q^{M}(m,n) = \begin{cases} 1, & \min(k_{m}, k_{n}) > k_{F} \quad \text{and} \\ & \max(k_{m}, k_{n}) > k_{M}, \\ 0, & \text{otherwise.} \end{cases}$$
 (2)

The model-space sp spectrum is defined self-consistently by

$$\varepsilon_k^M = t_k + u_k^M, \tag{3}$$

where t_k is the kinetic energy and the sp potential is

$$u_k^M = \begin{cases} \sum_{h < k_F} \langle kh | G^M(\omega = \varepsilon_k^M + \varepsilon_h^M) | kh \rangle, \ k < k_M, \\ 0, \qquad k > k_M. \end{cases}$$

$$(4)$$

The above MBHF approach is a generalization of the well-known BHF approach, the latter corresponding to a special case of the former with $k_M = k_F$

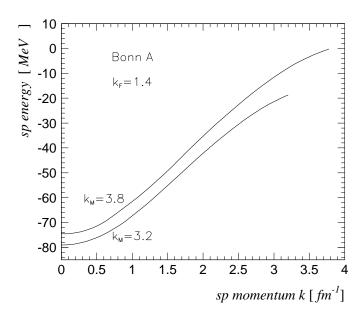


Fig. 1. The MBHF sp potential u_k^M shown for different values of k_M using the Bonn A potential $(k_F = 1.4 \text{ fm}^{-1})$.

and commonly referred to as "standard" BHF. For the BHF method, only the kinetic energy (free particle spectrum) is included in the sp energy for momenta greater than k_F , while below k_F the sp potential u_k^M is included as well. In the MBHF method, the corresponding boundary is at k_M , beyond which one uses the free-particle spectrum. The BHF and MBHF sp energies are constructed so that they are always real. To ensure this property, we need to require that the MBHF spectrum $\epsilon^M(k)$ has a sp potential u_k^M which is always attractive. (Otherwise the propagator in G^M will have poles, leading to a complex G^M .) In Fig. 1, we show the sp potential u_k^M for some typical values of k_M . Similar results are obtained using the other potentials. Generally speaking, when k_M is small the sp potential is attractive. As k_M increases, the MBHF sp potential becomes more repulsive. For $k_M = 3.8 \text{ fm}^{-1}$, u_k^M is still attractive for small k, but becomes less attractive for larger k and is close to zero at $k = k_M$. For $k_M > 3.8 \text{ fm}^{-1}$, the sp potential becomes repulsive. When this happens, we will have a crossing between the free particle spectrum and the MBHF spectrum. This will in turn give rise to a sp potential which is no longer real, unless some ad hoc procedure is imposed such as suppressing its imaginary part. To prevent such crossings, we have chosen $k_M \sim 3.8 \; {\rm fm^{-1}}$ as an upper bound for k_M , which defines our model space. This caveat ensures that the MBHF G-matrix is always real.

The MBHF approach is basically an intermediate scheme, in the sense that only two-particle scattering states outside the model space are accounted for. This means that both particles must have momenta larger than k_F and that at least one of the fermions in the two-particle wave function has momentum larger than k_M . The model space Pauli operator defined in Eq. (2) exclude scattering states with both momenta below k_M . In the lowest order, MBHF calculations for the nuclear matter binding energy is performed in two steps. First, Eqs. (1) and (3) are solved self-consistently. In the second step a "standard" Brueckner type calculation (see Eq. (5) is performed except that the MBHF spectrum defined in Eq. (4) is used for $k_F < k < k_M$.

2.2 MBHF Results

We have performed lowest order MBHF calculations for various k_M values within the upper bound $k_M = 3.8 \text{ fm}^{-1}$. In Fig. 2 we present the average energy per particle as a function of k_M for three typical Fermi momenta, using the Bonn A and C potentials. For small Fermi momenta ($k_F = 1.2$ fm⁻¹) the results for the Bonn A potential are very insensitive to the choice of k_M . For a wide region of k_M (2.0-3.5 fm⁻¹) the energy variation is less than 0.5 MeV. For larger Fermi momenta we see that the variation is somewhat stronger, however, we find a "saturation" behaviour in the vicinity of $k_M \approx$ $3.0fm^{-1}$. This is a fortunate and desirable result. Here we have a minimum for E/A and moreover it is here that E/A seems to be least sensitive to k_M . Thus we believe that $k_M = 3.0 \text{ fm}^{-1}$ is an optimum choice for the MBHF calculations using the Bonn A potential. Note that intermediate states with large momentum components ($k > 3 \text{ fm}^{-1}$ are induced by the short-range part of the NN interaction [4,21,22]. Thus, using $k_M \approx 3.0 \text{ fm}^{-1}$ the intermediate states induced by the short-range repulsion are included in the model space Gmatrix. For the Bonn C potential we get very similar results, although there is a slightly larger k_M -dependence than for the A potential. For both potentials we find that E/A varies no more than 0.5 MeV for k_M between 2.5 fm⁻¹ and 3.2 fm⁻¹. Similar results are also found for the Bonn B potential.

One has to keep in mind that the strengths of the tensor force of the potentials discussed are different, as Bonn A contains the weakest tensor force component of the three potentials considered, while Bonn C contains the strongest one. Since all three potentials reproduce the same set of scattering data, a potential containing a weaker tensor component needs a strong central component. Intermediate states induced by the tensor force are relatively more strongly dominated by lower momentum components than states induced by the central force[9]. Therefore, one can expect that the energy contribution from scattering into states with momentum components lower than k_M will be larger for potential C than for A. This is also reflected in the larger k_M -

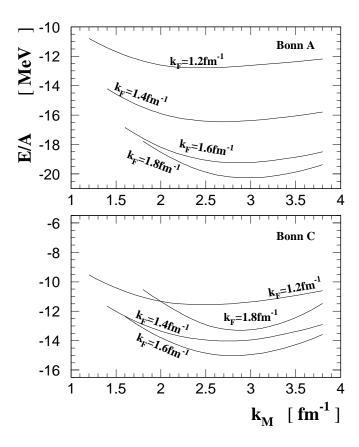


Fig. 2. Average energy per nucleon as a function of k_M for MBHF calculations using version A and C of the Bonn potentials. The results are for four typical Fermi momenta.

dependence in the calculations using potential C. The results using the other potentials are very similar and we find that it is a good approximation to use the model-space boundary $k_M = 3.0 \text{ fm}^{-1}$ for all potentials considered. In Fig. 3 the saturation points for calculations using $k_M = 3.0 \text{ fm}^{-1}$ are indicated by filled symbols while the saturation points from standard BHF calculations, which correspond to $k_M = k_F$, are indicated by open symbols. We see that the MBHF approach yields about 3 MeV additional binding energy compared to the BHF approach. The saturation density is slightly increased. The results show the well-known fact that within lowest-order Brueckner theory one is not able to reproduce the empirical data for nuclear matter. In the next section the MBHF method is extended to include additional many-body terms, such as the PPHH diagrams.

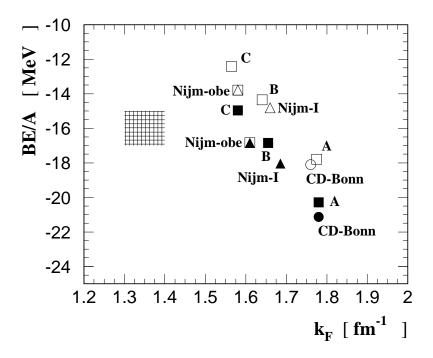


Fig. 3. Nuclear matter saturation points obtained in BHF calculations (opens symbols). MBHF calculations using $k_M = 3.0 \text{ fm}^{-1}$ are indicated by filled symbols. The results using versions A, B and C of the Bonn potential are shown by squares while the results for the charge dependent Bonn potential (CD-Bonn) are indicated by circles. The triangles represent the results using Nijmegen potential type I (Nijm-I) and the results from the Nijmegen meson exchange version (Nijm-OBE) are denoted by triangle+square.

3 Summation of Particle-particle and Hole-hole Diagrams for Nuclear Matter

The details of the PPHH-diagram method for nuclear matter can be found elsewhere [5]. However, to facilitate the presentation and discussion of our present work, we will give a brief review of the method. In perturbative approaches to nuclear matter, the well-known BHF theory has been the standard starting point. The effective two-body interaction in nuclear matter has then been given by the so-called G-matrix, which includes all ladder-type diagrams with particle-particle intermediate states to infinite order. However, in terms of the G-matrix it is nevertheless only a lowest-order theory. Other many-body contributions like screening terms or more complicated many-body terms are missing. The ground-state energy shift ΔE_0 in terms of the G-matrix is represented by the first-order diagram of Fig. 4 and reads

$$\Delta E_0^{BHF} = \sum_{ab} n_a n_b \langle ab | G^{BHF}(\omega = \epsilon_a + \epsilon_b) | ab \rangle.$$
 (5)

In Eq. (5) the n's are the unperturbed Fermi-Dirac distribution functions, namely $n_k = 1$ if $k \le k_F$ and = 0 if $k > k_F$ where k_F is the Fermi momentum. The sp energies are denoted by ϵ , and are determined self-consistently using the BHF theory.



Fig. 4. First order contribution to the ground-state energy shift ΔE_0 in BHF theory.

The Brueckner-Hartree-Fock G-matrix G^{BHF} contains repeated interactions between a pair of "particle" lines, as illustrated by the diagrams of Fig. 5. Note that they are so-called Goldstone diagrams, with an explicit time ordering. The third-order diagram (α) of Fig. 5 is given by

$$Diag.(\alpha) = \left(\frac{1}{2}\right)^3 \frac{V_{abmn}V_{mnrs}V_{rsab}}{(\epsilon_a + \epsilon_b - \epsilon_m - \epsilon_n)(\epsilon_a + \epsilon_b - \epsilon_r - \epsilon_s)}.$$
 (6)

Here m, n, r, s are all particle lines, and V_{ijkl} represents the anti-symmetrized matrix elements of the NN interaction V.

To the same order, there is also a diagram with hole-hole interactions, as shown by diagram (β) in Fig. 6, where a, b, r, s are all hole lines. This diagram is not included in standard BHF calculations of nuclear matter, for the following reason. In earlier times, nuclear-matter calculations were based on, by and large, the so-called hole-line-expansion. The essence of the hole-line approach is that diagrams with (n+1) hole lines are generally much smaller than those with n hole lines. With this criterion, diagram (β) which has 3 (independent)

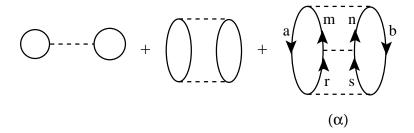


Fig. 5. Goldstone diagrams contained in the Brueckner-Hartree-Fock G-matrix G^{BHF} .

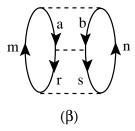


Fig. 6. Goldstone diagram with repeated interactions between hole lines.

hole lines would be negligible compared with diagram (α) which has 2 hole lines. Thus the former can be neglected. This approximation has, however, not been rigorously checked. To investigate the validity of this criterion, it may be useful to actually calculate diagrams like (β) .

A motivation behind the PPHH-diagram method of nuclear matter is also to include diagrams with hole-hole correlations like diagram (β). In so doing, the above time-ordered formalism is no longer convenient. We need to use the Green's function formalism, where all time variables are integrated over the same time interval from $-\infty$ to ∞ . Diagrams (α) and (β) are both time ordered diagrams. In the Green's function formalism, the sum of these two diagrams becomes a single diagram, namely diagram (γ) of Fig. 7. Note that we choose to draw Green's function diagrams differently from the time-ordered ones. The diagram of Fig. 7 is given by

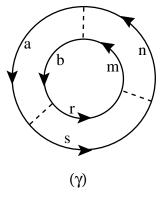


Fig. 7. Green's function diagram discussed in text. The states denoted by r and s can either be particles or holes.

$$Diag.(\gamma) = \frac{-1}{2\pi i} \int_{-\infty}^{\infty} d\omega e^{i\omega 0^{+}} \times tr[\frac{1}{3} F_{ab}(\omega) \bar{V}_{abmn} F_{mn}(\omega) \bar{V}_{mnrs} F_{rs}(\omega) \bar{V}_{rsab}], \tag{7}$$

where F represents the free PPHH Green's function

$$F_{ab}(\omega) = \frac{(1 - n_a)(1 - n_b)}{\omega - (\epsilon_a + \epsilon_b) + i0^+} - \frac{n_a n_b}{\omega - (\epsilon_a + \epsilon_b) - i0^+},\tag{8}$$

and \bar{V} is related to V by

$$\bar{V}_{abcd} \equiv \frac{1}{2} V_{abcd}. \tag{9}$$

In the above, the symbol tr (trace) means that all indices are summed over.

The advantage of using this Green's function formalism is that all the PPHH diagrams, of the general structure shown by Fig. 7, can be expressed in a simple algebraic form. In fact the entire PPHH-diagram series of this type becomes

$$"PPHH" = \frac{-1}{2\pi i} \int_{0}^{1} \int_{-\infty}^{\infty} d\omega e^{i\omega 0^{+}} tr[F(\omega)\bar{V}]$$

$$+ \frac{1}{2} (F(\omega)\bar{V})^{2} + \frac{1}{3} (F(\omega)\bar{V})^{3} + \cdots]$$

$$= \frac{-1}{2\pi i} \int_{0}^{1} \frac{d\lambda}{\lambda} \int_{-\infty}^{\infty} d\omega e^{i\omega 0^{+}} tr[F(\omega)\bar{V}\lambda]$$

$$+ (F(\omega)\bar{V}\lambda)^{2} + (F(\omega)\bar{V}\lambda)^{3} + \cdots]. \tag{10}$$

Here, we have introduced the integration over the parameter λ , in order to cast the summation over all terms into a simple geometrical series, without the factors $\frac{1}{2}$, $\frac{1}{3}$ and so forth.

The above expression is not yet suitable for nuclear-matter calculations. As is well known, the free NN interaction has a very strong repulsive core. The above series, expressed in terms of V, is not well defined as each of its terms is very large. A standard way to overcome this difficulty is to convert the above series into a series in the terms of the G-matrix. Song $et\ al.\ [5]$ have shown that within the model space approach the PPHH-diagram series can be rewritten in terms of G-matrix vertices. For example a third-order G-matrix PPHH diagram is given by the diagram of Fig. 7, with each of its dotted-line

interactions replaced by a G-matrix interaction. In this way, the contribution of the entire PPHH-diagram series to the nuclear-matter ground-state energy can be rewritten as

$$\Delta E_0^{PPHH} = \int_0^1 d\lambda \sum_{m \in (A-2)} \sum_{abcd \in P} Y_m(ab, \lambda) Y_m^*(cd, \lambda)$$
$$\langle ab|G^M(\omega = E_m|cd\rangle, \tag{11}$$

where P denotes the chosen model space, within which all nucleons are restricted to have momentum less than k_M . The G^M and ϵ^M are the model-space G-matrix and sp spectrum defined in Eqs. (1) and (3), respectively. To obtain the latter equation, a contour integration closed in the upper ω -plane, see Ref. [5] for further details, has been performed. Moreover, since by construction the model-space BHF G-matrix has no poles for negative energies ω , one avoids thereby imaginary contributions to the energy. This is perhaps the main advantage of the model-space approach for calculating the PPHH diagrams compared with the SCGF method of Dickhoff, Polls and Ramos [1]. However due to this approach, as stated previously, there are other observables of great interest which one is not able to calculate within the present scheme, namely one-body Green's function, spectral functions and momentum distributions.

Note that the above expression is rather similar to the BHF expression of Eq. (5). There the weighting factors are $n_a n_b$ and the G-matrix is evaluated at an energy $(\epsilon_a + \epsilon_b)$. Here the weighting factors are YY^* and the G-matrix is evaluated at energies E_m . The transition amplitudes Y and energies E_m are given by the RPA equation

$$\sum_{ef} [(\epsilon_i^M + \epsilon_j^M) \delta_{ij,kl} + (1 - n_i - n_j) \lambda G^M(\omega)] Y_m(ef, \lambda)$$

$$= \mu_m(\omega, \lambda) Y_m(ij, \lambda), \qquad (12)$$

with the self-consistent condition

$$\omega = \mu_m(\omega, \lambda) \equiv E_m. \tag{13}$$

For notational economy we will write $\mu_m(\omega, \lambda) = \mu_m$.

It is important to mention that the normalization of the RPA wave functions Y is given by

$$\sum_{ab} (1 - n_a - n_b) Y_m(ab, \lambda) Y_m^*(ab, \lambda) = \frac{-1}{1 - \frac{\partial \mu_m}{\partial \omega}|_{\omega = \mu_m}}$$
(14)

where $\mu_m \equiv \mu_m(\omega, \lambda)$. For $\lambda = 1$, E_m and Y_m of Eq. (12) are both physical quantities [20], namely

$$E_m = (E_0^A - E_m^{A-2}), (15)$$

and

$$Y_m(\alpha\beta) \equiv \langle \Psi_0^A | a_\alpha^+ a_\beta^+ | \Psi_m^{A-2} \rangle \tag{16}$$

where E_0^A and Ψ_0^A represent the energy and wave function of the nuclear matter ground state, and similarly E_m^{A-2} and Ψ_m^{A-2} the m'th state of the nuclear matter system with two less nucleons.

Eq. (12) is a standard RPA secular equation for the PPHH Green's function, and as shown its irreducible vertex function is given by the two-body model-space G-matrix G^M only. This is, however, inadequate in order to describe the Green's function, as there are also one-body terms in the PPHH vertex function. Such one-body diagrams are important for the PPHH Green's functions (see ref. [20] and references quoted therein). To first order in G^M , we should also include in the vertex function one-body diagrams. The resulting vertex function, denoted by Γ , is then composed of the three diagrams of Fig. 8. Here diagram (a) is the two-body G^M term, while diagram (b) is the one-body G^M term. We have added and then subtracted a one-body sp potential u^M to the Hamiltonian, namely $H = T + V = (T + u^M) + (V - u^M) \equiv H_0 + H_I$. Diagram (c) of Fig. 8 is the $-u^M$ term.

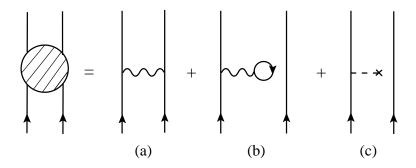


Fig. 8. Structure of PPHH vertex function Γ used to calculate PPHH diagrams in this work. The two-body part is the model space G-matrix G^M (a). Diagram (b) is the one-body term from G^M and diagram (c) is the one-body potential introduced u^M in the Hamiltonian.

The above concern about the vertex function suggests that for nuclear matter calculations we should consider a generalized PPHH-diagram series, as repre-

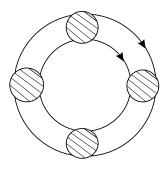


Fig. 9. An example of PPHH diagrams included in our calculations.

sented by Fig. 9. There each "blob" represents the vertex function Γ of Fig. 8. In this way the nuclear-matter PPHH diagrams include not only two-body interactions via G_M but also one-body insertions. The all-order sum of these generalized PPHH diagrams can still be readily performed, with the final result still given by Eq. (9), except that the amplitudes Y and energies E are now given by a modified RPA equation, namely

$$\sum_{ef} [(\epsilon_i^M + \epsilon_j^M) \delta_{ij,ef} + (1 - n_i - n_j) \lambda \Gamma(\omega)] Y_m(ef, \lambda)$$

$$= \mu_m(\omega, \lambda) Y_m(ij, \lambda). \tag{17}$$

A computational subtlety may be mentioned. The above RPA equation are to be solved with the self-consistent condition (13). It is rather complicated to do so numerically, and it was mainly because of this consideration that earlier calculations [5] treated this self consistency by way of a perturbation method. In the present work we have treated this self-consistency exactly.

The inclusion of the one-body insertions for the PPHH diagrams has played an important role in our calculation. When such insertions are included, the wound-integral effect is present in the PPHH-diagram calculation. Because of the interaction among nucleons, particularly the short range correlation among them, nucleons in the model space are part of the time outside the model space. This "absence" from the model space is represented by the wound integral. At low density, the wound integral is generally small and the normalization factor in Eq. (14) of the RPA amplitudes is close to -1. As the density increases, the wound-integral becomes larger and the normalization can become much smaller, such as -0.8. As a result, the PPHH-diagram contribution to the nuclear matter potential energy, as given by Eq. (11), is suppressed as density increases. In short, the inclusion of the one-body insertions has been essential for the determination of the nuclear matter saturation density, as has been observed in ref.[5].

As mentioned earlier, the PPHH diagrams are calculated within the model space P, where all nucleons are restricted to have momentum up to k_M . A main concern has been what value for k_M one should use. In section 2 we have pointed out that k_M should not exceed 3.8 fm⁻¹. For $k_M = k_F$, the PPHH-diagram approach reduces to the standard BHF method. Thus the range for k_M is between k_F and 3.8 fm⁻¹.

4 Results of PPHH-diagram Calculations

We have performed PPHH-diagram nuclear matter calculations for a range of k_M values within the above upper bound. For each k_M value, we first calculate the MBHF sp spectrum for various Fermi momenta (k_F) . Then we solve the RPA equation in Eq. (12) for several values of λ . The resulting wave functions Y and eigenvalues E are then used to evaluate the PPHH-diagram sum in Eq. (11). In Fig. 10 the average energy per particle E/A is shown as a function

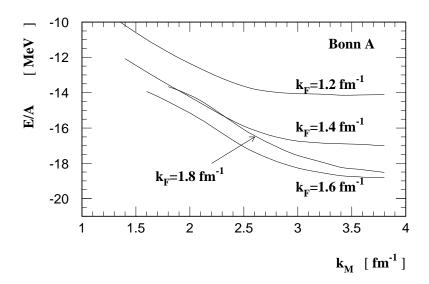


Fig. 10. The average energy per nucleon as a function of k_M for fixed values of k_F . The results are obtained with the version A of the Bonn potential.

of k_M for four typical Fermi momenta using version A of the Bonn potential. The results are quite stable with variations in k_M in the vicinity of $k_M = 3.8 \text{ fm}^{-1}$. The corresponding results using the Bonn B and C potentials are shown in Figs. 11 and 12, respectively. We see that the results using Bonn A and B are very similar, suggesting that $k_M = 3.8 \text{ fm}^{-1}$ is an optimal choice for calculating PPHH diagrams. However, for the Bonn C potential saturation occurs at higher k_M values.

To understand this difference it may be instructive to investigate contributions

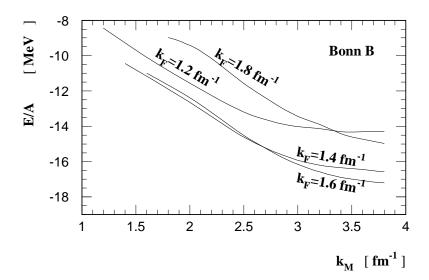


Fig. 11. Results for the version B of the Bonn potential. See Fig. 9 for further explanations.

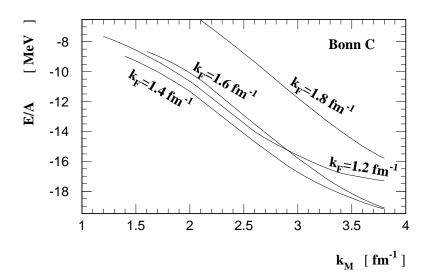


Fig. 12. Results for the version C of the Bonn potential. See Fig. 9 for further explanations.

from the different partial waves. In Fig. 13 the contributions from the ${}^{3}S_{1}+{}^{3}D_{1}$ channel are shown. Results obtained with the Bonn C potential are shown by solid lines. Comparing these curves with those in Fig. 12, we see that most of the energy gained when going from a low to a high k_{M} value comes from this channel. Note that in this channel the tensor force plays an essential role.

In the ¹S₀ channel, where the tensor force does not contribute, the energy shift

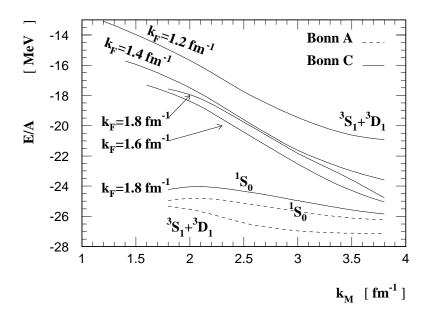


Fig. 13. Contributions to the average energy per particle from different partial waves. The results are obtained with the Bonn A and C potentials. See Fig. 10 for further explanations.

is found to be much smaller. In Fig. 13 the $^{1}S_{0}$ contribution is shown for $k_{F} = 1.8 \text{ fm}^{-1}$ For the other Fermi momenta this channel yields similar results. The k_{M} -dependence of the $^{1}S_{0}$ channel arises mainly in the normalization factors of Eq. (14). Thus, the k_{M} -dependence in the $^{1}S_{0}$ channel can be explained mainly by the ω -dependence of the vertex function Γ in RPA equation (17). Recall that ω -dependent one-body terms are included in Γ . When the RPA equation (17) is decomposed into separate partial wave channels, the one-body terms for the various channels are equal.

For higher order partial waves the (e.g., $l \ge 4$) ω -dependence of the G-matrix is known to be very weak and the G-matrix differs little from the bare interaction. Therefore, the k_M -dependence for all higher order partial waves is mainly due to the ω dependent one-body terms and shows up in the normalization factor.

For comparison we have also included the ${}^3S_1 + {}^3D_1$ and 1S_0 contribution for potential A. We see that the ${}^3S_1 + {}^3D_1$ channel for this potential has a much weaker k_M -dependence. Note that the Bonn A potential has a weaker tensor force than the Bonn C potential. This indicates that the strength of the tensor force is important for the k_M -dependence of the calculations. In the 1S_0 channel potentials A and C yield similar results. The small difference can be explained by the one-body terms of potential C which generally have a stronger ω -dependence than those of potential A. This is reflected in different normalization factors for the two potentials.

To complete our results we have included results for the CD-bonn potential

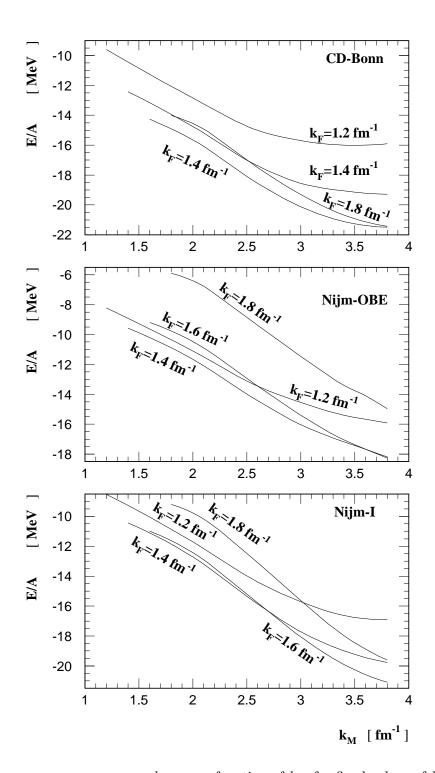


Fig. 14. The average energy per nucleon as a function of k_M for fixed values of k_F . Results are obtained with the CD-Bonn, Nijm-OBE and Nijm-I potentials.

[14] and two versions of the Nijmegen group [15], the meson-exchange potential (Nijm-OBE) and a local potential with a non-local contribution to the central force, i.e. the model Nijm-I of Ref. [15]. The results are shown in Fig. 14. We see that the results are similar to those using the earlier versions of the Bonn

potential, in the sense that when the strength of the tensor force increases, the stability of the results as functions of k_M worsens.

We find that the BHF calculations for Bonn B and Nijm-I yields similar results. Note, however, that the tensor force is stronger for the Nijm-I potential. The D-state probability of the deuteron reflects the tensor force in the NN-potential. The prediction from the Nijm-I potential is 5.66~% while the Bonn B and C potentials yields 5.0~% and 5.6~% respectively. Thus, the tensor force for the Nijm-I may be more comparable with that of the Bonn C potential. This is also reflected in the large PPHH-diagram contribution for the Nijm-I potential.

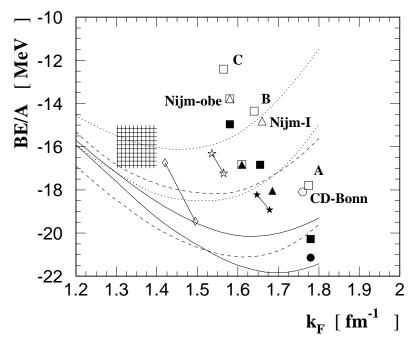


Fig. 15. Nuclear matter saturation curves (PPHH-diagram calculations) and points obtained with various potentials. The solid curves are obtained with the CD-Bonn potential, while dotted and dashed curves are obtained with the Nijm-OBE and Nijm-I respectively. For each potential calculations using $k_M = 3.0$ fm⁻¹ (upper curve) and $k_M = 3.8$ fm⁻¹ (lower curve) are presented. For the Bonn A, B and C potentials the saturation points (filled star, open star and diamond respectively) are shown for the two k_M values considered. In addition the MBHF results are presented as in Fig. 3.

In Fig. 15 we show the results of our PPHH-diagram calculation using $k_M = 3.0$ fm⁻¹ and 3.8 fm⁻¹. As seen from the figure the saturation density increases slightly when k_M increases to 3.8 fm⁻¹. However, compared to the MBHF results all our PPHH-diagram calculations yield a lower saturation density. Previous PPHH-diagram calculations for nuclear matter were performed using $k_M = 3.2$ fm⁻¹ [5,13]. We find that our calculations using the same k_M value yield similar results. Note that in this work the normalization of the RPA wave function is performed by the use of Eq. (14). In earlier calculations[5]

a perturbation method has been used in order to normalize the RPA wave functions.

5 Calculations for Neutron Matter

We have found that the results for the PPHH-diagram calculations are very sensitive to the strength of the tensor force. In symmetric nuclear matter the contribution from the tensor force to the binding energy comes mainly from the ${}^{3}S_{1}+{}^{3}D_{1}$ channel which has isospin equal to zero. For neutron matter, however, this channel does not contribute, and therefore the tensor force is not so important. To complete our discussion of the PPHH diagrams we therefore include results for neutron matter as well. In Fig. 16 we show the average

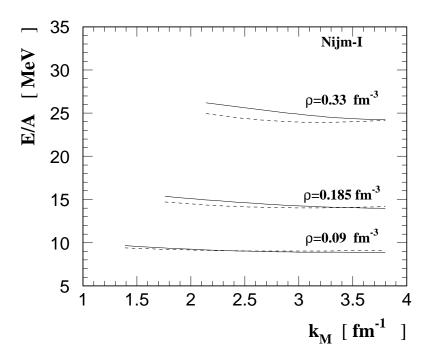


Fig. 16. The average energy per neutron for neutron matter as a function of k_M for various densities. The MBHF results are shown by dashed lines while the results including PPHH diagrams are shown by solid lines.

energy per nucleon as a function of k_M for various densities. In this figure we show only results for the Nijm-I potential, since the other potentials gave qualitatively similar results. The results from the PPHH-diagram calculation are given by solid lines. For the MBHF results, which are shown by dashed lines, the energy does not shift more than about 1 MeV if k_M increased from its lowest value ($k_M = k_F$) to $\approx 3.0 \text{ fm}^{-1}$. We see that the k_M -dependence is very

weak in both the MBHF calculations and the calculations including PPHH diagrams. Moreover, the contribution from PPHH diagrams are substantially reduced compared to the results for symmetric nuclear matter.

In Fig. 17 the average energy is plotted as a function of density for the three potentials. Results including PPHH diagrams are shown. However, we find that the contribution from the PPHH diagrams is small. This has important consequences for studies of neutron star properties. Many-body terms such as hole-hole terms play a smaller role. It is therefore of interest to perform a self-consistent calculation of particle-hole diagrams, of importance for long-range effects, in order to assess the relation between particle-particle, hole-hole and particle-hole terms in neutron matter or β -stable matter calculations.

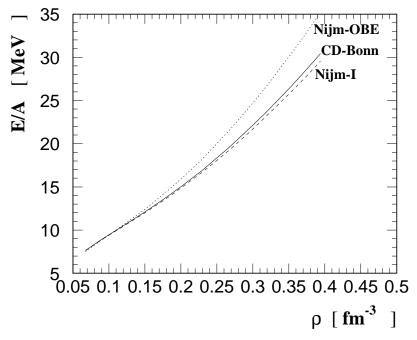


Fig. 17. The average energy per neutron for neutron matter using various potentials. PPHH diagrams are included using $k_M = 3.8 \text{ fm}^{-1}$. The results obtained with the CD-Bonn potential are shown by the solid line while the results using Nijm-OBE and Nijm-I potentials are shown by dotted and dashed lines respectively.

6 Summary and Conclusion

A central ingredient in the PPHH-diagram calculation for nuclear matter is its model space size k_M . How to determine it has been a long standing problem. We have carried out extensive nuclear matter calculations, with various choices for k_M for both the model-space Brueckner-Hartree (MBHF) approach and the approach which includes particle-particle and hole-hole (PPHH) diagrams. We

have found that for the MBHF approach the nuclear matter binding energy and saturation density vary little with k_M for k_M in the vicinity 3.0 fm⁻¹. The location of this saturation region for k_M is almost independent of the potential used.

For calculations including PPHH diagrams we find a saturation region where the nuclear matter binding energy and saturation density vary rather little with k_M for $k_M \approx 3.8~{\rm fm}^{-1}$. However, the calculations including PPHH diagrams exhibit a stronger k_M -dependence than the MBHF calculations. Our results have shown that the strength of the tensor force is important for the k_M -dependence. Potentials with weak tensor force yield better convergence for large k_M than those with stronger tensor force.

The new potentials which have a χ^2 fit per datum close to 1 generally yield similar results as the older versions of the Bonn potentials. For all potentials considered, the saturation density is substantially reduced when PPHH diagrams are included.

MBHF calculations for neutron matter are found to be insensitive to the choice of k_M . Moreover, the contribution from PPHH diagrams is found to be small in this case. Thus, combining this with our result for symmetric matter, we have shown that the contributions from PPHH excitations in a nuclear medium depend strongly on the tensor force component of the NN interaction.

We have carried out our PPHH-diagram calculations using the MBHF sp spectrum. It should be of interest to employ other sp spectra in the summation of PPHH diagrams for nuclear matter calculations. As an example, it would be desirable to employ a sp spectrum which is obtained in a consistent way from the PPHH-diagram calculation of the binding energy. As far as we know, how to formulate such a sp spectrum is not yet fully understood. Such a formulation is presently being studied by us.

Acknowledgements

This work has been supported by The Research Council of Norway (NFR) under the Programme for Supercomputing through a grant of computing time.

References

- [1] A. Ramos, A. Polls and W. Dickhoff, Nucl. Phys. A 503 (1989) 1.
- [2] A. Ramos, W. Dickhoff and A. Polls, Phys. Rev. C 43 (1991) 2239.

- [3] W. Dickhoff and H. Müther, Rep. Prog. Phys. 55 (1992) 1947.
- [4] Z.Y. Ma and T.T.S. Kuo, Phys. Lett. B127 (1983) 137; T.T.S. Kuo and Z.Y. Ma, Nucleon-Nucleon Interaction and Nuclear Many-body Problems, eds. S.S. Wu and T.T.S. Kuo (World Scientific, Singapore, 1984) p. 178; T.T.S. Kuo, Z.Y. Ma and R. Vinh Mau, Phys. Rev. C33 (1986) 717. Phys. Rev. C 29 (1984) 1207.
- [5] H.Q. Song, S.D. Yang and T.T.S. Kuo, Nucl. Phys. A 462 (1987) 491.
- [6] J.P. Jeukenne, A. Lejeune and C. Mahaux, Phys. Rep. 25 (1976) 83; C. Mahaux,P.F. Bortignon, R.A. Broglia and C. H. Dasso, Phys. Rep. 120 (1985) 1.
- [7] V.R. Pandharipande and R.B. Wiringa, Rev. Mod. Phys. 51 (1979) 821; S. Fantoni and V.R. Pandharipande, Nucl. Phys. A 427 (1984) 473.
- [8] H. Kümmel, K.H. Lührmann and J.G. Zabolitzky, Phys. Rep. 36 (1978) 1.
- [9] R. Machleidt, Adv. Nucl. Phys. 19 (1989) 189
- [10] R. Brockmann and R. Machleidt, Phys. Rev. C 42 (1990) 1965.
- [11] B.D. Serot and J.D. Walecka, Adv. Nucl. Phys. 16 (1986) 1.
- [12] M. Jaminon and C. Mahaux, Phys. Rev. C 41 (1990) 697.
- [13] M.F. Jiang, T.T.S. Kuo and H. Müther, Phys. Rev. C38 (1988) 2408.
- [14] R. Machleidt, F. Sammarruca and Y. Song, Phys. Rev. C 53 (1996)
- [15] V.G.J. Stoks, R.A.M. Klomp, C.P.F. Terheggen and J.J. de Swart, Phys. Rev. C 49 (1994) 2950.
- [16] R.B. Wiringa, V.G.J. Stoks and R. Schiavilla, Phys. Rev. C 51 (1995) 38.
- [17] R.B. Wiringa, R.A. Smith and T.L. Ainsworth, Phys. Rev. C 29 (1984) 1207.
- [18] G.E. Brown and R. Machleidt, Phys. Rev. C 50 (1994) 1731.
- [19] M. Hjorth-Jensen, T. T. S. Kuo and E. Osnes, Phys. Reports 261 (1995) 125.
- [20] S.S. Wu and T.T.S. Kuo, Nucl. Phys. A430 (1984) 110.
- [21] B.D. Day, Rev. Mod. Phys. 39 (1967) 719.
- [22] M.I. Haftel and F. Tabakin, Nucl. Phys. A158 (1970) 1.